
CHALMERS
UNIVERSITY OF TECHNOLOGY

# Proton irradiation-induced cracking and microstructural defects in UN and (U,Zr)N composite fuels

Journal of Materiomics 10 (2024) 906–918

Contents lists available at ScienceDirect

Journal of Materiomics

journal homepage: www.journals.elsevier.com/journal-of-materiomics/

Research paper

# Proton irradiation-induced cracking and microstructural defects in UN and (U,Zr)N composite fuels

Elina Charatsidou [a, *], Maria Giamouridou [a], Andrea Fazi [b], Gyula Nagy [c], Diogo Ribeiro Costa [a, d], Sarmad Naim Katea [c, e], Mikael Jolkkonen [a], Gunnar Westin [c], Mattias Thuvander [b], Daniel Primetzhofer [c], Pär Olsson [a]

[a] KTH Royal Institute of Technology, Stockholm, Sweden
[b] Chalmers University of Technology, Gothenburg, Sweden
[c] Uppsala University, Uppsala, Sweden
[d] Westinghouse Electric Sweden AB, Västerås, Sweden
[e] Höganäs Sweden AB, Höganäs, Sweden

ARTICLE INFO

*Article history:*
Received 6 November 2023
Received in revised form
27 January 2024
Accepted 31 January 2024
Available online 8 March 2024

*Keywords:*
Proton irradiation
Uranium nitride
Spark plasma sintering
Irradiation induced cracking
Simulated burn-up structure
Composite nuclear fuels

ABSTRACT

Proton irradiation with a primary ion energy of 2 MeV was used to simulate radiation damage in UN and (U,Zr)N fuel pellets. The pellets, nominally at room temperature, were irradiated to peak levels of 0.1, 1, 10 dpa and 100.0 dpa resulting in a peak hydrogen concentration of at most 90 at. %. Microstructure and mechanical properties of the samples were investigated and compared before and after irradiation. The irradiation induced an increase in hardness, whereas a decrease in Young's modulus was observed for both samples. Microstructural characterization revealed irradiation-induced cracking, initiated in the bulk of the material, where the peak damage was deposited, propagating towards the surface. Additionally, transmission electron microscopy was used to study irradiation defects. Dislocation loops and fringes were identified and observed to increase in density with increasing dose levels. The high density of irradiation defects and hydrogen implanted are proposed as the main cause of swelling and consequent sample cracking, leading simultaneously to increased hardening and a decrease in Young's modulus.



## 1. Introduction

Uranium Nitride (UN) is a promising nuclear fuel candidate for future advanced nuclear reactor systems [1–3]. Generation IV lead-cooled fast neutron reactors (LFRs), such as the SUNRISE-LFR and SEALER-55 designed in Sweden, as well as BREST-300 in Russia, are planned to operate on UN or (U,Pu)N fuel [4–6]. Due to its properties, UN offers enhanced performance and the potential of a closed fuel cycle. UN exhibits properties such as high uranium density [1,7], good thermal conductivity [8–10], high melting temperature [11], compatibility with liquid metal coolants [12], good breeding performance [12,13], and reprocessing capabilities [1].

Although in the literature there are several studies on irradiation of UN fuel [14–18], they were typically conducted over two decades ago. These studies were limited to moderate neutron fluences, resulting in limited characterization providing detailed information on microstructural and mechanical changes of UN under irradiation. Furthermore, these studies did not describe how the irradiation tolerance is affected by the presence of solid fission products (FP). It is challenging, expensive and cumbersome to investigate neutron irradiation effects on new fuel concepts, essentially due to the worldwide shortage in nuclear reactors worldwide accepting irradiation tests. Neutron irradiation introduces additional complexities, such as long irradiation times, high costs and sample activation, necessitating the use of dedicated hot-cell facilities to perform post-irradiation examination.

For these reasons, ion-irradiation was employed here to further the knowledge on irradiation performance. Proton irradiation provides rapid material damage, associated with lower costs, shorter irradiation times and is much more readily accessible given

* Corresponding author. Physics Department, Nuclear Science and Engineering, KTH Royal Institute of Technology, 10691, Stockholm, Sweden.
*E-mail addresses:* elinach@kth.se (E. Charatsidou), polsson@kth.se (P. Olsson).
Peer review under responsibility of The Chinese Ceramic Society.

https://doi.org/10.1016/j.jmat.2024.01.014

the availability of several ion irradiation facilities. Moreover, proton irradiation offers a well-controlled environment where single variable dependencies can be studied, which is particularly important when planning separate effect tests. Lastly, ion-irradiation allows for flexibility in control of temperature, dose, and dose rate, which is not easily achievable with neutron irradiation in a nuclear reactor [19]. Proton irradiation on nuclear fuels has been predominantly used to study $UO_2$ so far [20–22]. Recently proton irradiation of UN-$UO_2$ composite system, was studied with a 2 MeV proton beam with fluences up to $8 \times 10^{18}$ ions·cm$^{-2}$, at 400 °C and 710 °C, respectively, in order to investigate the microstructural evolution of the U–N–O system [23,24]. The studies concluded that proton irradiation induced dislocation loops, oxidation, and phase transformation, as with increased temperature, the presence of $UO_2$ and $U_2N_3$ phases was increased, and the amount of UN was decreased.

The objective of the present work is to bridge the gap in the limited data on irradiation behavior of UN and the lack of information on the behavior of solid FP effects on the UN matrix under irradiation. Hence, a campaign was performed to irradiate UN and a simulated burn-up (SIMFUEL) fuel pellet with a proton beam reaching damage doses up to 100 displacements per atom (dpa) at a dose rate of 0.005 dpa/s. A (U,Zr)N SIMFUEL pellet is included in this investigation since zirconium (Zr) is one of the representative and significant solid FPs that need to be considered, as it plays a vital role in fuel behavior. The impact of Zr on irradiation-induced cracking and microstructural defects in UN was evaluated. The Stopping and Range of Ions in Matter (SRIM) [25] software was employed to simulate the proton irradiation characteristics in UN and the composite SIMFUEL. The hydrogen concentration profile, peak damage doses as well as proton penetration depth were simulated. Following the irradiation campaign, a wide range of characterization techniques was employed to study microstructural, and mechanical properties of the samples prior and post-irradiation as well as to investigate irradiation-induced defects such as cracking, hardening, and extended defects.

## 2. Methods

### 2.1. Powder synthesis and pellet fabrication

High purity UN powder was fabricated by the hydriding-nitriding-denitriding method using uranium metal obtained from the Institutt for Energiteknikk, Norway, employing the experimental set up and temperature profile described by Malkki *et al.* [26]. The average particle size of UN powders produced by this method was around 5 μm [27–29]. Elemental analysis was carried out to determine the levels of oxygen and nitrogen in the UN powder, using a LECO TC-436DR Nitrogen/Oxygen Analyzer.

The ZrN nano-phase powder used to fabricate the SIMFUEL pellet was synthesized by a novel carbothermal nitridation route using $N_2$ gas as nitrogen source and sucrose as reducing agent. The process yielded nano-particle sized *c*-ZrN with an average crystal size of 87 nm and a lattice parameter of $a = 0.4598$ nm. The synthesis process and complete characterization of the ZrN powder is given elsewhere [30].

To produce the desired concentration of SIMFUEL composites and enhance mixing and homogenization, UN and ZrN powders were milled using a Retsch PM100 milling machine at an inert argon atmosphere. The final mixing step, before sintering, was performed with a hand mixing bowl using an agate piston and a mortar. The as-synthesized powders were sintered using Spark Plasma Sintering (SPS) [31] in a Dr. Sinter SPS 530 ET machine, connected with a glovebox allowing for a transfer of the powders under inert, argon, atmosphere. The powders were filled into graphite dies lined with thin graphite paper to avoid powder-carbon interaction during sintering. The sintering was performed at the National SPS Facility at Stockholm University. Both pellets were sintered under low vacuum (<10 Pa) and the heating rate was set to 100 °C/min until the maximum sintering temperature, 1,650 °C, was reached. A pyrometer was used to measuring temperature at the outer surface of the die. After sintering, the graphite paper was ground off the pellets' surfaces using SiC paper (grit 280 to 2000) and polished with diamond suspensions (9, 3, 1 μm and 0.25 μm). The pellets were then polished using colloidal silica suspension of 0.04 μm, and washed in an ultrasonic bath for 30 min.

### 2.2. Damage calculations

#### 2.2.1. Proton-induced damage

To understand displacement damage in UN caused by neutrons, proton irradiation was implemented in this work. Since the existing literature on irradiation studies of UN fuel is scarce, before proceeding with the proton irradiation, SRIM was used to produce predictions of the proton irradiation damage profile in UN and the composite $(U_{0.9}Zr_{0.1})N$ fuel pellet. The "Ion Distribution and Quick Calculation of Damage" mode was implemented for these calculations based on [32]. The SRIM results were used to estimate the total damage (in dpa) onto the sample as well as the depth at peak irradiation dose and the hydrogen implantation profile.

In most earlier studies using proton irradiation of nuclear fuels, the energy of the protons has been chosen to be around 2 MeV [21–23,33]. Therefore, for all simulations, and the irradiation experiments, the proton energy was set to 2 MeV. For simulating UN in SRIM, a layer with two elements was created, with 50 at.% nitrogen and 50 at.% uranium. The displacement threshold energies were set to 40 eV for uranium and 25 eV for nitrogen [23]. Similar to UN, when simulating the composite $(U_{0.9}Zr_{0.1})N$ fuel pellet, three concentrations were defined: 50 at.% nitrogen, 45 at.% uranium and 5 at.% zirconium. The displacement threshold energy for zirconium was set to 35 eV [34]. The lattice and surface binding energies were set to zero for each of the chosen layers and the total number of ions simulated was $10^6$.

The scanning nuclear microprobe facility at the Tandem Laboratory at Uppsala University was used for the irradiation experiments [35]. Both UN and $(U_{0.9}Zr_{0.1})N$ pellets underwent proton implantation using 2 MeV energy. A pressure of approximately $10^{-7}$ bar was maintained in the high-vacuum chamber during the irradiation. The experiment was conducted at room temperature. The pellets were mounted onto a sample holder controlled through a 3-axis step motor with the help of a light microscope. The choice of irradiation fluences can be largely attributed to the irradiation time needed to achieve the desired doses.

Four areas (spots) were irradiated in each sample, with various fluences $\varphi$ chosen to scan a range of irradiation conditions of reactor relevance, considering the experimental limitations. The size of the first three irradiation areas of the UN sample was 12 μm × 12 μm, while 10 μm × 10 μm was used for spot 4 of UN as well as all four spots of the SIMFUEL pellet. While irradiating UN, the average current of the proton beam was 1.5 nA, however, while irradiating the composite sample, it varied between 0.2 nA and 1.5 nA among the four irradiation fluences.

It is of interest to estimate the temperature in the irradiation volume, as samples could experience thermal shock due to beam heating. Calculations were performed considering the beam energy, ion fluences, irradiation times, depth of implantation and irradiation areas. The total power received at the irradiation spot was obtained and finite element modelling (FEM) was used to evaluate the thermal response of the UN fuel pellet during irradiation. The COMSOL Multiphysics® tool was used to estimate the temperature distribution of the fuel pellet during irradiation. The

geometry and parameters of the fuel pellet were constructed introducing the UN thermal properties [9]. A constant heat flux was applied on a 10 μm × 10 μm area at the center of the pellet. Heat loss by radiation from the pellet surface was applied. Since the surface emissivity of UN is not known, a constant surface emissivity of 0.5 was selected as an average approximation. The pellet temperature distribution was estimated in a time-dependent simulation covering the entire irradiation time. It is important to mention that the FEM simulations assume only heat loss through radiation (as a conservative case). Heat loss by conduction from the sample to the holder will decrease the temperature of the irradiation volume even further. The power from the proton beam on the irradiation areas can be calculated since the beam intensity, beam energy and irradiation areas are known. The FEM results show that, even in the conservative simulated case, the beam does not cause significant heating of the sample, with a maximum temperature increase of less than 10 °C in the beam spot compared to the rest of the pellet. Therefore, the irradiation does not cause significant heating in the pellet.

### 2.3. Characterization

A combination of characterization techniques was employed to study the samples before and after proton irradiation to gain insights into the evolution of the phase composition, crystal structure, surface morphology, mechanical properties, microstructure, and irradiation-induced defects.

X-ray Diffraction (XRD) was used to provide information on phase presence and lattice parameters of the UN powder, pellet and $(U_{0.9}Zr_{0.1})N$ composite fuel pellets. The Siemens D5000 X-Ray Diffractometer was used, with a Cu $K_\alpha$ target at a 40 mA current and 35 kV voltage. The XRD patterns were collected in the $2\theta$ angle range of 20° to 100°. The step size was set to 0.02°, and the acquisition time was 2 s per step for the powder and 0.5 s per step for the pellets. For the solid pellets, the sample stage was set to a rotation speed of 15 r/min. The Rietveld refinement was performed using the PROFEX [36] software and the Crystallography Open Database (COD) [37].

Scanning Electron Microscopy (SEM) (Hitachi S-3700 N) was used to examine the surface morphology, while Energy Dispersive Spectroscopy (EDS) enabled elemental composition analysis. The ImageJ software was used to investigate and measure surface features, such as pores and macro irradiation defects [38].

Electron Backscattering Diffraction (EBSD) data was obtained using a JEOL JSM-7800F SEM equipped with a Bruker e-Flash detector. The EBSD images provided details on grain boundaries, orientation, and size. Electrons of 20 keV electrons and an iterative data cleaning process were used. A total of 30 iterations from 8 to 5 nearest neighbors were performed, with an indexing rate above 90%. The equivalent circle diameter was chosen as grain size, and the pixel and grain thresholds were set to 50 pixels and 15°, respectively.

Atomic Force Microscopy (AFM) with a Dimension FastScan AFM-Bruker allowed for high-resolution and three-dimensional surface characterization. With AFM it was possible to study surface irradiation defects and identify areas of interest for further investigation with Transmission Electron Microscopy (TEM). The AFM was operated in tapping mode, and an AIO-Al cantilever of rectangular shape was used, with length, width, and thickness equal to 150, 30 μm and 2.7 μm respectively, and a constant surface tension of 7.4 N/m with an aluminum tip. The image analysis was done using the NanoScope Analysis 1.9 software.

Nano-indentation using a Femto-Indenter FT-104 measured nanohardness and Young's modulus. Continuous Stiffness Measurement (CSM) was used and a grid of 8 × 8 indents was arranged with a 2 μm distance between each indent in both $x$ and $y$ directions. Displacement-controlled mode was selected, and the maximum penetration depth of the indents was set to 0.2 μm, with a total applied load time set to 10 s.

Focused Ion Beam (FIB) was utilized to extract thin lamellae for TEM analysis, providing insight into the nanoscale bulk microstructure. The TEM specimens were lifted out from the fuel pellets with a dual-beam focused ion beam/scanning electron microscope (FIB/SEM) in an FEI Versa 3D workstation implementing standard procedures for in-situ sample lift-out and specimen preparation [39]. Conventional transmission electron microscopy TEM (CTEM) was performed on an FEI Tecnai T20 operated at 200 kV. Scanning TEM–energy dispersive X-ray spectroscopy (STEM-EDS) mapping and point analysis were performed on a TESCAN GAIA3 – FIB/SEM workstation equipped with a X-Max$^n$ EDS detector from Oxford Instruments. Further STEM imaging and EDS mapping were performed on an FEI Titan 80–300 operated at 300 kV equipped with an X-sight detector from Oxford Instruments. During sample preparation, protective platinum (Pt) was deposited on the top of the surface to minimize possible damage and/or contamination of the area of interest [40]. After the Pt deposition, Ga milling was carried out to thin the samples, starting from a voltage of 30 kV and later reduced to 5 kV to limit the ion damage to the surface of the lamellae. A reference lamella, 20 μm wide and 5 μm deep, was extracted from both samples to characterize the material prior to irradiation. Larger lamellae, 20 μm deep, were lifted out for irradiated regions of both the UN and the SIMFUEL sample to include the regions with peak irradiation damage in the TEM cross-sections.

## 3. Results and discussion

### 3.1. Phase composition and microstructure of as-fabricated materials

UN powders previously fabricated *via* the hydriding-nitriding-denitriding process, split into three consecutive fabrication days, have measured around 1,600 wt $\times 10^{-6}$ of oxygen. Oxygen is mostly present as $UO_2$, and was there on average 1.2 wt% [28,41]. In this work the UN powder production was performed in a modified way, introducing a continuous 17 h fabrication process. The oxygen concentration was measured, by LECO, to be 135 wt $\times 10^{-6}$, resulting in a $UO_2$ concentration of 0.13 wt%, an order of magnitude improvement in purity level from the reference above. The average nitrogen concentration was determined by LECO to be 5.5 wt%. The XRD pattern of the UN powder is shown in Fig. 1 (top). The pattern demonstrates a single-phase cubic structure corresponding to a lattice parameter of $a = (0.4889 \pm 0.0001)$ nm, which is in good agreement with previously reported UN lattice parameters [28,42,43]. Additionally, the refinement revealed a low oxygen concentration of 1.45 wt% $UO_2$ and 98.55 wt% UN. It can be noted that XRD and LECO analyses yield somewhat different results. XRD points to a higher oxygen presence, which might result from XRD overestimating phases of low concentrations due to background noise. The elemental analysis by LECO is more accurate and reliable at such low percentages.

The sintering properties of UN by SPS have been studied previously [29]. SPS chosen here to achieve a fully dense pellet without introducing significant changes to the grain size. The same sintering parameters were applied to the composite sample, which resulted in a sintered yet cracked pellet along its axial direction throughout its bulk. This crack behavior can be explained by the difference in thermal expansion of the two source powders, UN and ZrN, resulting in non-uniform expansion and shrinkage during heating and cooling, respectively, which could have caused the

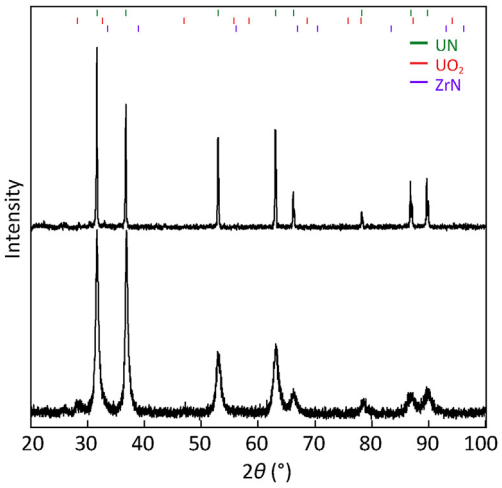


**Fig. 1.** XRD patterns of UN as-synthesized powder **(top)** and sintered $(U_{0.9}Zr_{0.1})N$ fuel pellet **(bottom)**.

observed cracking. Hence, to avoid this, the sintering pressure was reduced to 45 MPa. To ensure a fully densified pellet, the reduction in holding pressure needs to be accounted for. Thus, the sintering time was increased to an additional 30 min, resulting in a fully dense, crack-free composite fuel pellet. Moreover, the increase in sintering time enhances the interdiffusion between UN and ZrN, which improves the homogeneity of the solid solution in the sample.

After sintering, the graphite paper was ground off the samples, and the pellet densities were measured by a modified Archimedes' method [27]. The sintering parameters of UN and $(U_{0.9}Zr_{0.1})N$, including sintering temperature, holding time, applied pressure, as well as the dimensions and final density, in terms of theoretical density (TD), of the pellets are shown in Table 1.

XRD was used to study the phase presence in the solid samples and to identify the lattice parameters of the UN and $(U_{0.9}Zr_{0.1})N$ composite fuel pellets. Rietveld refinement revealed that the UN pellet has a lattice parameter of $a = (0.4893 \pm 0.0001)$ nm, which is in good agreement with the source powder and with values reported in the literature [28,44,45]. Additionally, the refinement showed a low oxygen concentration of 0.08 wt.%, resulting in 0.68 wt.% $UO_2$. The oxygen concentration appears to be lower in the UN pellet compared to the value obtained for the UN powder, 1.45 wt.% of $UO_2$. The opposite could be expected, since the powder handling outside the inert atmosphere of a glove box should have increased, or at least maintained, the oxygen content in the pellet. Therefore, it can be concluded that XRD does not appear to exhibit high accuracy, at such low concentrations. This is an additional reason why the LECO method is preferred to determine phase concentrations below 1% (in mass).

Analysis of the XRD pattern obtained for the composite fuel sample, Fig. 1 (bottom), revealed the presence of a single phase with the peaks situated at the same $2\theta$ angles as for UN, however, broader in width. The lattice parameter was determined to be $a = (0.4883 \pm 0.0001)$ nm. This value indicates that the ZrN has formed a solid solution with UN, where Zr has replaced U atoms in the UN lattice, reducing the lattice parameter. Furthermore, the refinement revealed an oxygen concentration of 0.15 wt.%, which is equivalent to 1.29 wt.% $UO_2$.

The lattice parameter of the composite sample, obtained from XRD, allowed for estimation of the percentage of ZrN in solid solution with UN by employing the Vegard's law [46], as shown in formula (3) below.

$$a_{A_{(1-x)}B_x} = (1-x)a_A + x \bullet a_B \quad (3)$$

$a_A$ and $a_B$ are lattice parameters of pure compounds UN ($a = 0.4893$ nm) and ZrN ($a = 0.4598$ nm) [30], respectively. $a_{A_{(1-x)}B_x}$ is the lattice parameter of the solid solution obtained in this section ($a = 0.4883$ nm). By substituting the lattice parameters above, $x$ can be calculated and was found to be $x = 0.034$, revealing that approximately 3.4 at.% of ZrN formed solid solution with UN. Therefore, the average chemical composition throughout the composite sample is $(U_{0.97}Zr_{0.03})N$.

SEM was used to obtain information on the sample surface morphology, such as grain structure and size, local porosity, and phase presence. Fig. 2 shows a backscattering electron image of the UN and $(U_{0.9}Zr_{0.1})N$ fuel pellets. The microstructure of the UN pellet consists of porosity present in the form of small pores, a homogeneous matrix of the single phase, with a few dark inclusions, located at the grain boundaries, which are related to $UO_2$. These areas were identified by EDS as oxide-rich regions. The sample surface was examined in detail, and the areas to be irradiated were carefully chosen to be representative. Hence, the irradiation spots were selected to be pore and oxide free to minimize the effects of porosity as well as oxide inclusion in the behavior of the UN fuel under irradiation. The average grain size, measured using the ImageJ software, was $(7.8 \pm 2.8)$ μm, which is in good agreement with previously reported values [28,29,47].

Regarding the microstructure of the composite $(U_{0.9}Zr_{0.1})N$, the oxide inclusions were similar to those in UN. EDS analysis suggests a solid solution matrix of U–Zr–N throughout the pellet, with an average concentration of Zr raging from 3 at.% to 4 at.%. This value agrees with the result by XRD and Vegard's law obtained above. The four regions to be irradiated were chosen to represent a homogeneous solid solution of (U,Zr)N and to avoid oxide inclusions. The average concentration of Zr present in these regions is equal to $(3.0 \pm 1.5)$ at% Zr corresponding to a solid solution of $(U_{0.97}Zr_{0.03})N$. The average grain size of this sample was $(5.2 \pm 1.7)$ μm. This value is smaller than the grain size obtained for pure UN. This observation can be explained since the ZrN powder used has nano-particle size, while the UN powder fabricated is of micron-particle size. Therefore, when both powders mix creating a solid solution throughout the matrix, as well as ZrN precipitates, the grain size value is an average of the grain size of UN, ZrN and (U,Zr)N. This results in an intermediate grain size value, which is higher than that of ZrN but lower than that of UN. The remaining Zr seems to precipitate as ZrN throughout the sample (dark areas in Fig. 2 (right)).

### 3.2. Nano hardness and Young's modulus

Nanoindentation is employed to study the mechanical behavior of UN and composite fuel samples. Both nanohardness and Young's modulus can be measured with this technique. The

**Table 1**
Sintering parameters for UN and $(U_{0.9}Zr_{0.1})N$ pellets.

| Sample | Sintering temperature (°C) | Sintering time (min) | Uniaxial pressure (MPa) | Density (%TD) | Diameter (mm) | Height (mm) |
|---|---|---|---|---|---|---|
| UN | 1,650 | 5 | 80 | 97.5 | 9 | 3.4 |
| $(U_{0.9}Zr_{0.1})N$ | 1,650 | 35 | 45 | 98.2 | 10 | 3.2 |

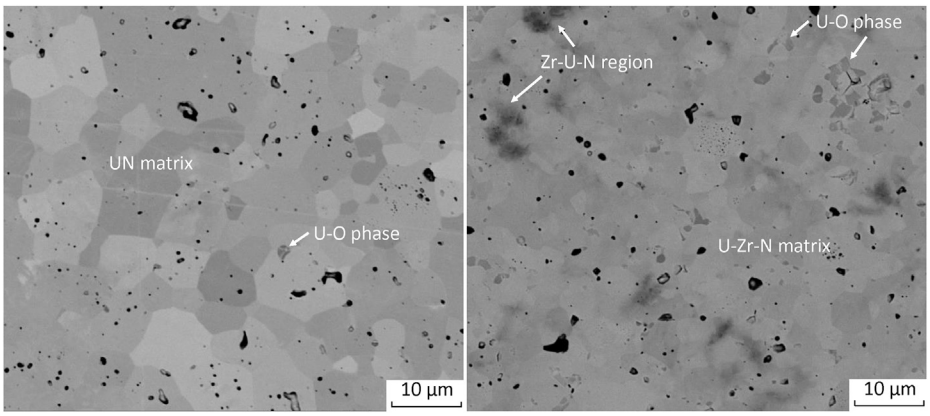


**Fig. 2.** Scanning electron images (BSE mode) of the sintered pellets: UN **(left)**, $U_{0.9}Zr_{0.1}N$ **(right)**.

nanoindentation was performed on both UN and $(U_{0.9}Zr_{0.1})N$ pellets, in a non-irradiated area as a reference. The same settings were then used to measure hardness and Young's modulus in the irradiated areas.

The nanoindentation equipment produces results of hardness and reduced Young's modulus, $E_r$. In order to compare the values of Young's modulus obtained in this work with the literature, formula (4) is used to calculate the Young's modulus of the samples, $E_s$ [48].

$$\frac{1}{E_r} = \frac{1-\nu_i^2}{E_i} + \frac{1-\nu_s^2}{E_s} \tag{4}$$

$E_i$ and $\nu_i$ are the Young's modulus and Poisson's ratio of the diamond tip indenter and are equal to 1,140 GPa and 0.07, respectively. $E_s$ and $\nu_s$ refer to the Young's modulus and Poisson's ration of the sample, and $E_r$ is the reduced Young's modulus, obtained by nanoindentation. The Poisson's ratio of UN is equal to $\nu_{UN} = 0.225$ [49] and of ZrN is, $\nu_{ZrN} = 0.25$ [50].

The Young's modulus of UN can be also calculated using formula (5) provided by Hayes *et al.* [49].

$$E = 0.258 \bullet D^{3.002} \bullet \left(1 - 2.375 \bullet 10^{-5} \bullet T\right) \tag{5}$$

where $E$ is the Young's modulus in MPa, $D$ is the pellet's density in % TD and $T$ is temperature in Kelvin. The relation is valid for $70\% \leq D \leq 100\%$ and $298\ K \leq T \leq 1{,}473\ K$.

The pellets were indented at a reference area, separate from the irradiation regions. With the help of SEM, the individual indents were analyzed, and the areas of indentation were studied, see Fig. 3 (**left**). Fig. 3 (**right**) depicts a color map of hardness in the 8 × 8 array of the individual 2 μm × 2 μm square indents. The variation in hardness and modulus values can mainly be attributed to the following two reasons. The depth of the individual indent, which will determine the measurement result, and the location of the indentation, which will alter the result, in case an indent hits inside a grain or at a grain boundary, as well as depending on the phase present in the indented region.

From Fig. 3 for UN, the hardness measurements lie within four color-coded clusters, with the green and yellow values being on the low end of the hardness. For UN, the indents corresponding to the lower hardness are mostly located at the top part of the 8 × 8 array, and as can be seen from the SEM image, most of these indents hit near or on pores, thus resulting in lower hardness values. From the same SEM image, the higher hardness values (orange and red squares), correspond to indents on pore-free regions. The average value of hardness of the UN sample was found to be (8.1 ± 0.2) GPa. Literature reports a hardness value of pure UN around 10 GPa [28,48,49].

For the composite sample, the results are split into four colored clusters indicating a variation in hardness, bottom right of Fig. 3. There are three green squares corresponding to hardness values that are lower than the rest of the clusters. After investigation under SEM, it was found that the indents at the 2–4 μm and 8–10 μm areas on the *X* axis hit pores, however, the indent at the 4–6 μm region on the *X* axis is located on a grain boundary. On the opposite side of the spectrum, there are four red squares which lie on the higher values of hardness. Even though the red indent located at the 2–4 μm region on the *X* axis, has an average-level Zr concentration and has visibly hit a pore, the hardness measurement is high in relation to the average. The cluster of three red indents located at 6–10 μm on the *X* axis revealed a Zr concentration ten times higher than the average, hence resulting in increased hardness. The average value of hardness of the SIMFUEL sample was found to be (9.1 ± 0.4) GPa. Since no literature reference is present for the nanohardness values of such a SIMFUEL composition, an estimation was made using Vegard's law. Using formula (3) and replacing the lattice parameter of UN and ZrN with the hardness of each phase respectively, the hardness of the SIMFUEL sample can be estimated, which was found to be between 8.5 GPa and 9.2 GPa for a 3 at.% and 10 at.% ZrN concentration, respectively. The hardness of the composite sample is higher than that of UN. This is expected since ZrN is harder than UN [51,52]. Therefore, a solid solution of (U,Zr)N would result in a hardness in between UN and ZrN, closer to that of UN since the concentration of ZrN is limited to 10 at.%.

The Young's modulus of UN follows the expected relationship of proportionality to hardness, meaning low hardness values correspond to low Young's modulus values, and higher hardness to higher Young's modulus. The measurement resulted in an average value of (224 ± 4.5) GPa for the reduced Young's modulus of UN. Formula (4) was used to calculate the Young's modulus, which was found to be 264 GPa. This result closely agrees with the reported literature values [28,48]. The correlation by Hayes *et al.* [49] for the Young's modulus of UN, formula (5), for a sample of 97.5% TD and at room temperature, results in a value equal to 240 GPa. Therefore, it can be inferred that the measured value in this work agrees with earlier results.

Lastly, the average reduced Young's modulus of $(U_{0.9}Zr_{0.1})N$ was measured to be (237 ± 4.5) GPa. The Young's modulus of the composite can be obtained from formula (4), however, formula (3) is necessary to approximate the Poisson's ratio of $(U_{0.9}Zr_{0.1})N$, by replacing the lattice parameter with the Poisson's ration of UN,

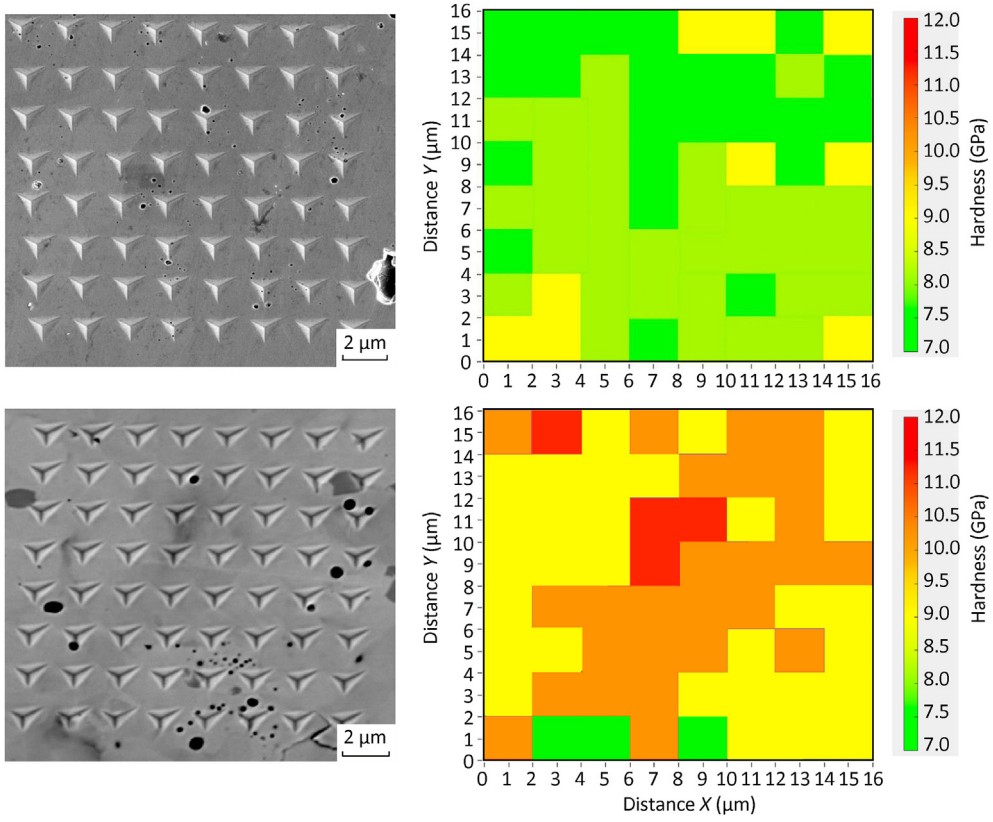


**Fig. 3.** SEM images of the indents **(left)** and color map for the 8 × 8 indent array **(right)** for UN **(top)** and $(U_{0.9}Zr_{0.1})N$ **(bottom)**.

$\nu_{UN} = 0.225$ [49], and ZrN, $\nu_{ZrN} = 0.25$ [50]. The result was found to be $\nu_{(U_{0.9}Zr_{0.1})N} = 0.228$ which leads to Young's modulus of $(U_{0.9}Zr_{0.1})N$ equal to 283 GPa. Thus, the results point to increased hardness and Young's modulus of a sample where ZrN is present. This is in close agreement with the Young's modulus of the composite pellet obtained using Vegard's law, for $E_{UN} = 264$ GPa (this work) and $E_{ZrN} = 460$ GPa [50], resulting in $E_{(U_{0.9}Zr_{0.1})N} = 284$ GPa.

### 3.3. Damage calculations

#### 3.3.1. Proton-induced damage

Simulation of the proton irradiation on UN and the composite fuel resulted in an estimate of the proton-induced damage profile as well as hydrogen concentration in the samples. Despite the addition of the ZrN powder in the UN, the peak damage dose obtained for both samples as well as the peak hydrogen concentration, was of the same level, while the depths of the peaks differ slightly. The peak dose corresponding to spot 1, 2, 3, and 4 is equal to 0.1, 1, 10, and 100 dpa, respectively. The peak hydrogen concentration for both samples is equal to 0.9 at.%, 8.0 at.%, 46.0 at.% and 90.0 at.% H for spot 1, 2, 3 and 4, respectively. It can be observed that the increase in hydrogen concentration is not linear with the dose, which is due to the fact that the peak concentration volume increases with increased fluences. The hydrogen concentration peak appears 1 μm deeper than the peak damage dose for both samples, and this could be attributed to the fact that after the ions create damage in the material, they continue to travel through the material's bulk with insufficient energy to cause any additional damage, before eventually stopping. The irradiation volume has been obtained from the full-width half maximum (FWHM) of the curve in Fig. 4 and found to be around 1,540 $\mu m^3$. It is important to note that in spot 4, as shown in Fig. 4, the peak hydrogen concentration is approaching 90 at.%, which is a very large concentration considering the small irradiation volume, since the hydrogen concentration peak is near zero close to the surface and concentrated around the peak irradiation region. Therefore, the irradiation-induced behavior of the samples is likely to be influenced by the hydrogen accumulation at the depth near 20 μm. However, it is improbable to see irradiation defects due to hydrogen pileup near the sample's surface. For UN the peak damage dose is found at 18.9 μm depth into the sample's bulk, however, the sample surface is experiencing ten times lower damage dose. For example, in spot 4, Fig. 4, the peak damage dose is approximately 100 dpa, at a depth of 18.9 μm, whereas near the surface the dose deposited is in the range of 10 dpa. For the $(U_{0.9}Zr_{0.1})N$ sample, the peak depth appears at 19.2 μm depth, since the stopping force of Zr is lower than that of U, increasing particle range.

### 3.4. Post-irradiation analysis

#### 3.4.1. Microstructure and surface morphology of irradiated pellets

The first two irradiation spots, with doses 0.1 dpa and 1 dpa, did not reveal any surface, microstructural or elemental difference before and after irradiation. Therefore, it was not trivial to pinpoint the exact post-irradiation region, since there was no clear indication of where the proton beam hit the sample. Hence, this work focuses on the 10 dpa and 100 dpa irradiation areas. For the 10 dpa (spot 3) and 100 dpa (spot 4), there were visible marks of the irradiation regions. For UN, in Fig. 5a the reference areas 3 and 4 are depicted before irradiation (dashed-line square), and the 10 dpa and 100 dpa regions are shown (solid-line square), with visible post-irradiation marks. The same areas are depicted in Fig. 5b for $(U_{0.9}Zr_{0.1})N$.

For UN, in Fig. 5a, at 10 dpa, the surface appears to be brighter

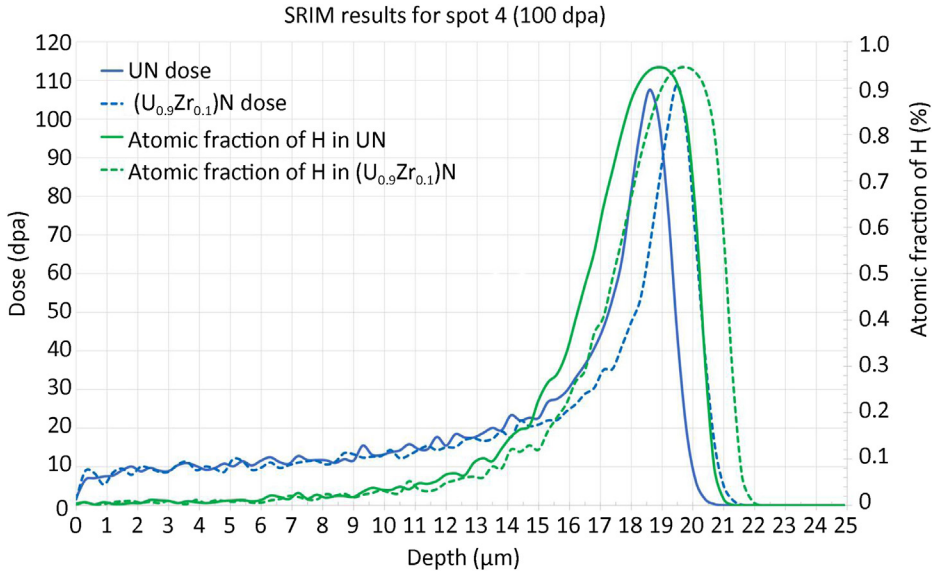


**Fig. 4.** SRIM simulation results for UN (solid lines) and $(U_{0.9}Zr_{0.1})N$ (dashed lines) for spot 4 with a fluence of $10^{20}$ ions·cm$^{-2}$ and a dose of 100 dpa.

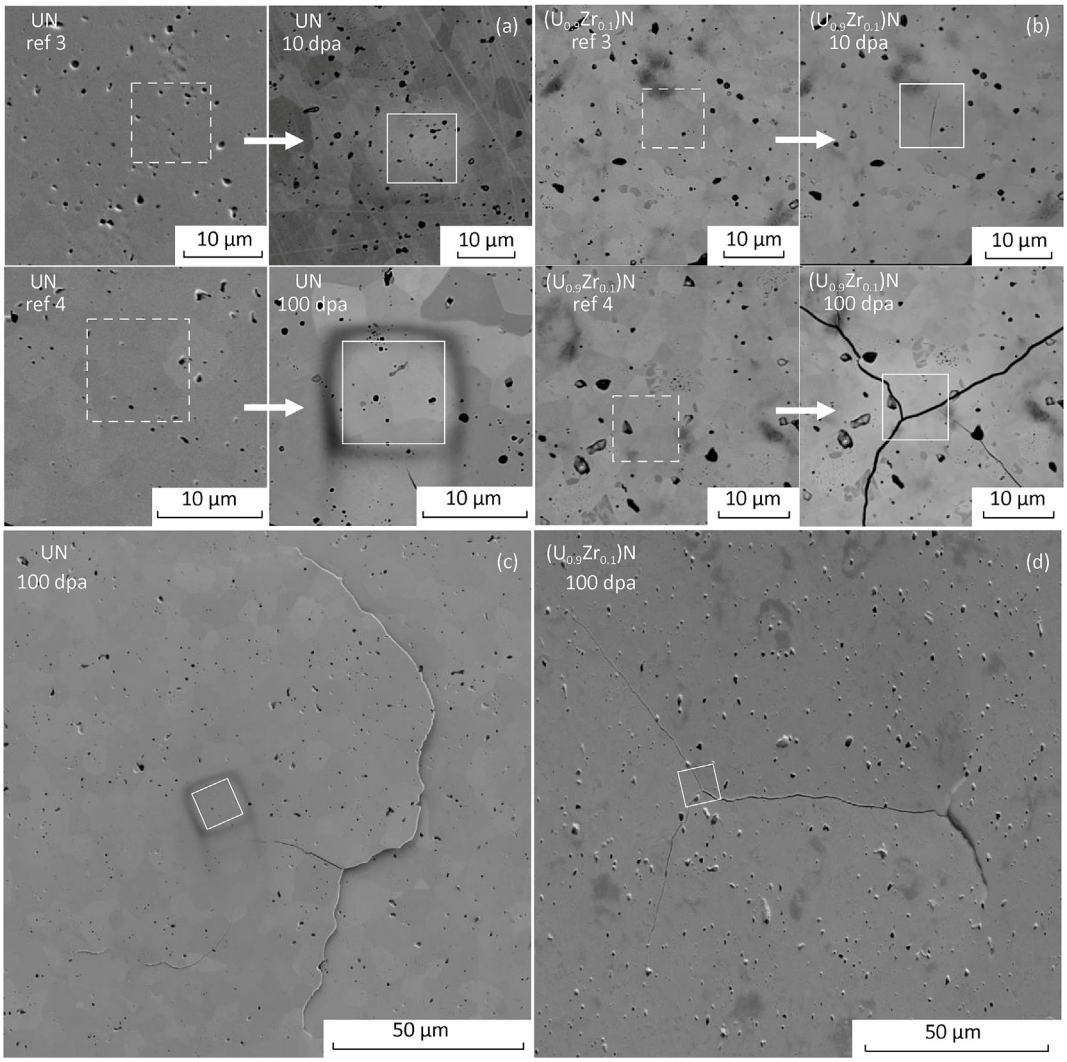


**Fig. 5.** SEM images of selected pre-irradiation reference areas marked with dashed squares and post-irradiation regions marked with solid squares for UN **(a)** and $(U_{0.9}Zr_{0.1})N$ **(b)**, for 10 dpa and 100 dpa; Overview of the crack in the 100 dpa irradiation region in UN **(c)** and $(U_{0.9}Zr_{0.1})N$ **(d)**.

under SEM, specifically under the BSE detector. The bright 'burn' mark is the size of the irradiated region, approximately 12 μm × 12 μm. Even though brighter regions under BSE indicate the presence of elements with higher atomic number compared to the surrounding area, the EDS analysis did not reveal any elemental composition changes in the irradiated region, but an increase C content was observed on the irradiation rim (Appendix A, Fig. A1). The 10 dpa region of the composite sample, Fig. 5b, differs from that of UN, for mainly two reasons. Firstly, the surface of the irradiated region does not appear to have a brighter mark under SEM, and the EDS analysis did not reveal any changes in the elemental composition of the irradiated region. Secondly, contrary to the crack-free spot 3 of UN, a 10 μm long crack can be observed on the composite sample. This can be explained since the presence of Zr increased the hardness of the SIMFUEL matrix, making it prone to more enhanced cracking behavior compared to the softer UN pellet. It is important to note that the bulk effect of irradiation is expected to be more severe, since the surface dose is one order of magnitude lower.

In the UN region that received 100 dpa, Fig. 5a, it can be observed that there is cracking initiated near the center of spot 4. Cracking also exists in the SIMFUEL pellet for the 100 dpa dose, Fig. 5b, however, the cracking is more extensive. For UN, the initial crack appears at an area which is elevated (swollen), compared to the sample surface and is approximately 30 μm long. The swelling and liftoff of the irradiated area and the region around it was observed with the help of a tilted stage under EBSD and can be seen in Fig. A2 in Appendix A. Similar swelling behavior was observed for the SIMFUEL pellet. The initial crack leads to a secondary crack propagating in two different directions (Fig. 5c). The secondary crack is over three times larger than the initial crack, approximately 150 μm long. Additionally, two smaller cracks can be observed on the left-hand side of the irradiation region. These smaller cracks are about 10 μm and 30 μm long and located approximately 50 μm away from the center of the irradiation. For the SIMFUEL sample, a similar yet exacerbated behavior as that of UN, is observed. A crack is initiated from the elevated (swollen) center of the irradiated region, extending in four directions. Additionally, the area covered by the total cracking pattern, Fig. 5d, is larger than the area of the crack in UN, since the crack in $(U_{0.9}Zr_{0.1})N$ that leads to the secondary crack is twice as long as that in UN. The secondary crack appears to be wider with a lot of material liftoff. This indicates that the secondary crack occurred rapidly and more aggressively, thus, breaking, and lifting off part of the material away from the surface bulk, leaving the unaffected material below.

From SRIM results the depth of the peak damage dose is similar for UN and $(U_{0.9}Zr_{0.1})N$ as is the profile of the hydrogen accumulation. Hence, both sample surfaces experience similar doses as well. By maintaining the same irradiation conditions for both samples, which resulted in both pellets cracking in a similar manner under 100 dpa it is proposed that crack formation is not coincidental and was caused, among others, due to irradiation. Therefore, it can be inferred that increasing the irradiation dose, the damage in the material is exacerbated, since no crack was visible in spot 3 of UN. The presence of extended surface cracking supports that there is a significant disruption deeper in the material, since the peak damage region is found at 18.9 μm depth from the surface, which experienced one tenth of the dose.

The grain properties of the UN and the $(U_{0.9}Zr_{0.1})N$ pellet were studied using EBSD. Fig. 6 demonstrates the band contrast and inverse pole figure of UN before and after receiving a dose of 100 dpa.

The analysis resulted in an average grain size of (7.1 ± 2.3) μm for UN and (5.2 ± 1.7) μm for $(U_{0.9}Zr_{0.1})N$. The grain size obtained here for UN and $(U_{0.9}Zr_{0.1})N$ are very close to the values obtained by SEM above. Additionally, Fig. 6 demonstrates a random distribution and no preferential crystallographic orientation of the grains for either sample. The grain and orientation results are in agreement with previous studies [29], where UN pellets were sintered with the help of SPS. Ref. [53] suggests that a preferential grain orientation could result in changes in material properties such as strength, ductility, and toughness, which in result could cause changes to the fuel performance [29]. Here, such an effect is not expected as there is no preferential crystallographic orientation.

Moreover, as the irradiation region was limited to an area of 100 $\mu m^2$ and since the average grain occupies an average area of about 40 $\mu m^2$, only a few grains, or parts of grains were included in the irradiated region. Thus, no information could be obtained regarding grain growth. Lastly, the irradiation-induced cracks in both samples feature combined cracking patterns, incorporating both transgranular and intergranular cracks, as cracks appear to propagate both through the grains and along the grain boundaries, respectively. AFM revealed that the irradiation rim was elevated with a high carbon presence (Appendix A, Fig. A1). This could result from residual hydrocarbons present in the high-vacuum environment, which are then sputtered away by the beam and get redeposited around the implanted area.

### 3.4.2. Irradiation-induced hardness and elasticity change

Nano-indentation measurements were performed on both samples, in the 100 dpa irradiated regions (spot 4), to study the effects of proton irradiation to the material's hardness and elasticity. The results for UN and $(U_{0.9}Zr_{0.1})N$ are presented in Fig. 7 (top), and Fig. 7 (bottom) respectively. The nanoindentation data for UN have been collected from a secondary 100 dpa region spot that was irradiated under the same conditions as described in Section 2.2.3.

From Fig. 7 (left), the SEM images show which of the indents in the 8 × 8 array are in the irradiated region. The white line marks the rim of the irradiation spot. The indents inside and on the rim represent the irradiation area and the rest are outside the irradiated region, yet still in the vicinity of the cracked region. For UN the SEM image revealed further cracking of the rim, due to the indentation, represented by the single green square in the red-square cluster. This green-marked indent will not be taken into consideration when calculating the hardness and Young's modulus of the irradiated region of UN, as it was a faulty measurement, and it is not representative of the material's properties. For the UN phase, the red cluster indicates the irradiated area, whereas the rest of the clusters belong to the un-irradiated region. The average value of the hardness and reduced Young's modulus for the irradiated UN were found to be (11.5 ± 0.9) GPa and (165.0 ± 8.4) GPa, respectively. The Young's modulus was calculated using formula (3), and found to be 183 GPa, for the irradiated region of UN. Compared to the reference region, the irradiation induced a hardness increase in UN [17]. The increase in hardness was 40% for the 100 dpa condition. On the other hand, the Young's modulus was reduced due to irradiation by 30% compared to its reference value.

For the composite pellet, the indents that belong to the irradiation region, cover the area of *X*: 0–6 μm and *Y*: 0–8 μm, in Fig. 7 (bottom). The two green indents, at *X*: 0–1 μm, *Y*: 0–4 μm, will not be counted towards the averages, as they hit inside the crack, thus are not representative of the irradiated bulk region. The average value of the hardness and reduced modulus for the irradiated $(U_{0.9}Zr_{0.1})N$ were calculated to be (11.5 ± 1.1) GPa and (177.0 ± 10.2) GPa, respectively. The Young's modulus is equal to 199 GPa. As observed previously, the hardness induced due to irradiation is increased here as well and is 26% higher. Similarly, to the findings of UN, the Young's modulus of the irradiated region of $(U_{0.9}Zr_{0.1})N$ is 30% lower than that of the reference region.

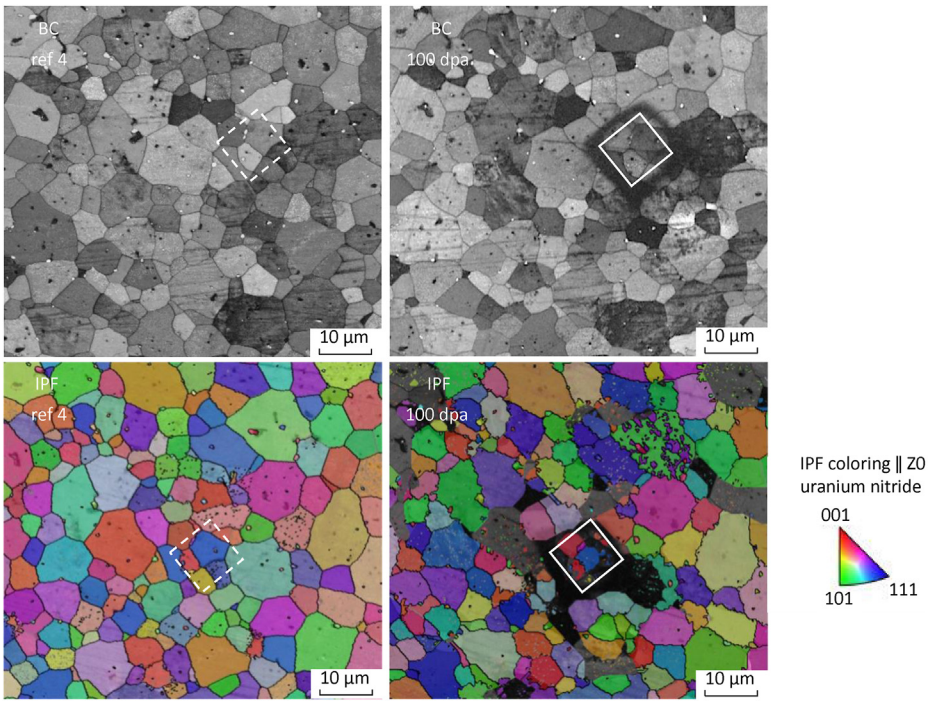


**Fig. 6.** EBSD analysis of the selected pre-irradiation reference area marked with dashed squares and the same region post-irradiation marked with solid squares for UN at 100 dpa (band contrast **(top)**, inverse pole figure **(bottom)**).

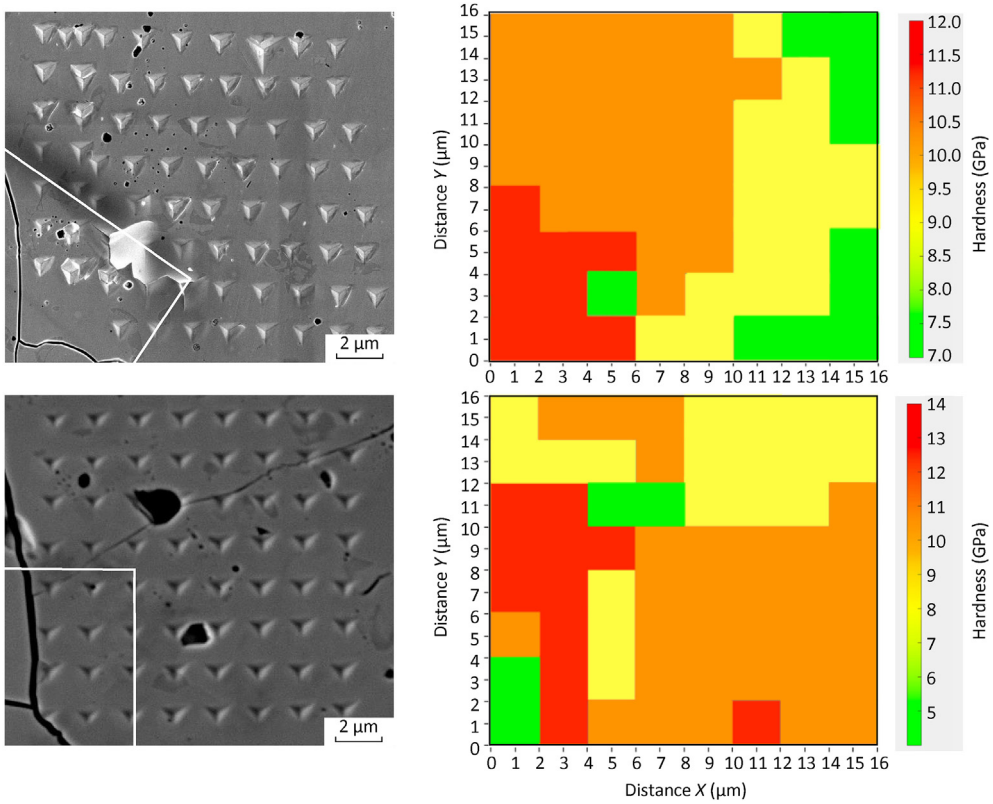


**Fig. 7.** SEM images of the indents **(left)** and color map for the 8 × 8 indent array **(right)** for UN **(top)** and $(U_{0.9}Zr_{0.1})N$ **(bottom)** at the 100 dpa irradiated area. The reader is advised to note the scale difference in the colormap between the two samples.

### 3.4.3. *Irradiation-induced bulk defects analyzed via TEM*

To investigate irradiation-induced bulk defects and identify the cracking mechanism, the 10 dpa and 100 dpa irradiation regions were studied under TEM. Additionally, reference lamellae were

lifted out, from both samples, to investigate pre-existing features and compare them with the irradiated samples to examine irradiation defects. The lamellae extracted were approximately 20 μm long and 5 μm and 20 μm deep for the reference and irradiated regions, respectively. Deeper lamellae were extracted for the irradiated areas to include the peak irradiation damage depth. During milling, the bulk of the material was revealed, and cracking was identified at the peak damage region, near 19 μm, for both the 10 dpa and the 100 dpa irradiation regions, in both UN and (U,Zr)N samples.

Fig. 8a depicts the 10 dpa and 100 dpa milled regions, in UN, featuring cracks parallel to the surface at a depth of the peak damage region. The same was observed in the SIMFUEL regions during milling. It is proposed that these cracks have propagated from the bulk, most damaged region, towards the surface. The presence of cracks in a consistent manner, at the peak implantation depth, calculated by SRIM, confirms that the material cracked due to high damage deposited from the irradiation in the region. The lamellae examined here can be seen in Fig. A3 in Appendix A, where no significant number hydrogen bubbles were observed, hence indicating that the main reason for cracking was local swelling due to damage induced into the material from the irradiation. The 10 dpa region of UN was the only one that did not reveal surface cracks. However, cracking could be observed at the peak damage region after milling. Since there was a surface crack observed in the 10 dpa irradiated region on the SIMFUEL, it can be inferred that the crack propagation was more rapid compared to that in UN. This can be attributed to the presence of Zr in the SIMFUEL, increasing the hardness and reducing the elasticity of the material, thus making it more susceptible to enhanced cracking under the same irradiation conditions.

Fig. 8b depicts the TEM images of the reference and irradiated lamellae of both samples. From the reference images, 0 dpa, it can be observed that there are several features pre-existing in the sample bulk before the irradiation. Dark spotting and possible dislocation lines (marked with white arrows) are visible in both reference images. Both UN and SIMFUEL appear to have similar homogeneous structures. Here the reference images are presented to facilitate comparison with the irradiated regions, as it was observed that previous literature on ion irradiated UN tends to report bulk results on irradiated samples and not reference areas [20,23,24], which does not give the possibility to compare between the two and makes it hard to attribute features to microstructure or irradiation, respectively.

The images referring to 1 dpa damage were taken from the spot 3 (peak damage of 10 dpa) lamellae, near the sample surface, where the damage dose is one order of magnitude lower. In the 1 dpa damage region, micro fissures can be observed in the UN sample (marked with white arrows), in Y-like formations, indicating intragranular micro cracking due to irradiation-induced swelling. The 1 dpa region of the SIMFUEL displays dislocation lines (marked with white arrows), similar to the ones observed in the unirradiated regions, thus classified as pre-irradiation existing features. Both reference and 1 dpa images are taken in the same

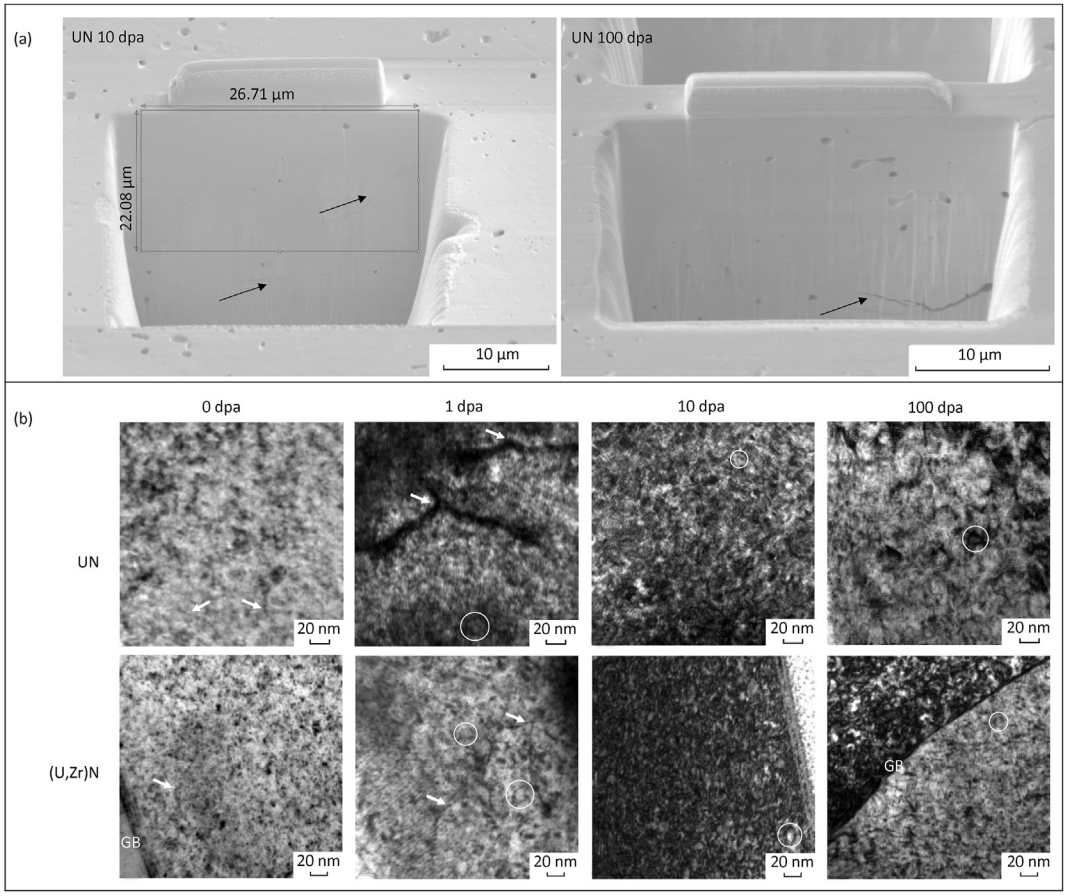


**Fig. 8.** (**a**) SEM - SE images of the milled irradiation regions of 10 dpa and 100 dpa in UN. The black arrows point to bulk cracks. (**b**) BF-TEM images of the reference and irradiated regions for both UN and SIMFUEL samples. The pictures marked as corresponding to 1 dpa dose were collected near the surface of the 10 dpa samples. The white arrows point to dislocation lines and micro fissures, whereas the white circles indicate dislocation loops. Where grain boundaries are visible, they are indicated by GB.

**Table 2**
Dislocation loop densities for the irradiated regions in UN and $(U_{0.9}Zr_{0.1})N$ lamellae.

| Sample | Dislocation loop densities ($\times 10^{21}$ m$^{-3}$) | | | |
|---|---|---|---|---|
| | 1 dpa (plateau) | 10 dpa (peak) | 10 dpa (plateau) | 100 dpa (peak) |
| UN | 0.7 | 20 | 11 | 26 |
| $(U_{0.9}Zr_{0.1})N$ | 5.0 | 50 | 30 | 80 |

magnification, and it can be observed that fringes are considerably more prominent in the irradiated samples but are not visible in the reference areas. Lattice fringes were observed in unirradiated regions only under higher magnification. The presence of Moire fringes in the irradiated samples points to lattice distortion from self-interstitial clusters and dislocation loops that form due to the irradiation damage. The 10 dpa and 100 dpa images were taken from the same lamellae, with relatively similar thickness. The fringes in these areas appear denser, clustered, and more defined compared to 1 dpa. This indicates that their density is greatly enhanced by an increased damage to the lattice.

Moving to clearly defined dislocation loops, a quantitative analysis of the dislocation loop density is proposed here. Dislocation loops can be observed in the irradiated images (several examples marked with white circles), indicating prevalent irradiation induced damage. The irradiated images of both samples, at 1 dpa, appear to be consistent with previous literature finding [23,24,33], where similar dislocation loops and defects were observed in irradiated uranium-nitrogen-oxygen system. In Table 2 the dislocation loop densities of the irradiated volumes are presented. It is important to note that there are two values of dislocation loop densities reported for the 10 dpa dose levels for both samples. The two dose levels refer to the bulk region of spot 3 (peak dose 10 dpa) and the near surface region of spot 4 (plateau dose 10 dpa).

From Table 2 it can be observed that the dislocation loop density increases one order of magnitude from 1 dpa to 10 dpa. At the 10 dpa irradiation dose the two values are indicative of the regions that the measurements were taken from. The 10 dpa (peak) is the region with peak damage and hydrogen concentration, in the bulk of spot 3, for both pellets. There, besides the irradiation induced defects, hydrogen is expected to concentrate, distort the lattice even further and interact with defects. A higher density of dislocation loops is observed at the peak versus the plateau conditions for the 10 dpa dose levels. At 100 dpa the dislocation loop density increases further, however, there is a dampened effect of the damage, with respect to the lower doses, indicating a tendency towards defect saturation. Such significant levels of microstructural damage are expected to swell the materials, as defects expand the lattice around them. This, alongside the lack of hydrogen bubbles present at the peak concentration depths, is a confirmation that the cracking behavior can be attributed to the local swelling at the peak concentration depth. The cracks can then propagate towards the sample surface.

The lower the Young's modulus, the less resistant the material is to elastic deformation. Therefore, a lower level of applied stress is sufficient to create the same amount of strain and elastically deform the material. Here both irradiated samples display a 30% decrease in Young's modulus when measured in the surface of the irradiation spot. This result agrees with previously reported literature findings, where according to Ref. [54], the Young's modulus, of silicon carbide, reduces with increasing point defect concentration. In addition, ref. [55] proposes that irradiation-induced cracking, in silicon carbide, decreases the Young's modulus even further. Given that there appears to be a general anti-correlation between swelling and Young's modulus evolution, this decrease in elastic response combined with the saturation of defects in the irradiated bulk, see Fig. 8, indicates significant levels of local swelling. In this work extensive irradiation-induced cracking was observed around the 100 dpa irradiated regions. Additionally, the damage generated in the samples' bulk is of a high concentration, given the small irradiation volume, which results in local swelling of the irradiation affected grains and thus cracking of the material initiated in the irradiated regions. The damage combined with the high concentration of implanted hydrogen could have resulted in an effective expansion of the lattice parameter which in turn would further reduce the Young's modulus.

It is important to consider an additional reason that could enhance cracking in the samples. During SPS sintering the central part of the pellet is hotter, thus, has greater thermal expansion than the rim. Upon cooling this leads to a tensile stress which is greatest at the center, and to a corresponding compressive stress at the rim. The model appears to be supported by the observation that such cracking from the sintering itself is less frequent if additional thermal insulation is applied to the die, reducing the rate of heat loss and hence the radial temperature gradient during sintering. Thus, the localized damaged microstructure, which should be significantly swollen, could have initiated the bulk cracking which propagated towards the surface, and this may have been aided due to residual stress in the SPS sintered pellets.

## 4. Conclusion

In this work, the effects of proton irradiation behavior of SPS sintered UN and (U,Zr)N fuel pellets were studied. Surface and bulk techniques were employed to identify microstructural irradiation defects and mechanical testing was implemented to measure the effect of irradiation on mechanical properties, such as hardness and Young's modulus for doses up to 100 dpa. One limitation of this work was the inability to produce SIMFUEL pellets in homogeneous solid solution through the sample. An additional experimental limitation is associated with the proton irradiation, and particularly beam time constraints, costs and sample activation. Therefore, 100 dpa was selected as the highest peak damage dose in the UN and SIMFUEL pellets.

The composite sample in this work presents a solid solution matrix, as well as Zr-rich regions, due to insufficient diffusion of Zr atoms into the UN. Post-irradiation nanoindentation testing revealed irradiation-induced hardening as well as a decrease of the Young's modulus, as compared with the unirradiated regions. The increase in hardness was around 40% for UN and 26% for the SIMFUEL sample. The Young's modulus decrease was consistent for both samples and was found to be 30%.

Detailed surface and bulk characterization confirmed sample cracking, initiated at the bulk of the material, where the peak damage dose was deposited. The cracking propagated through the bulk and onto the sample surface. Examining the high density of defects present at the 10 dpa and 100 dpa irradiated bulk regions, it can be inferred that the main driving force for crack initiation was the substantial damage, in terms of defects and lattice distortion, deposited into the sample. The irradiation damage combined with high hydrogen concentration, given the relatively small irradiation volume, resulted in local swelling of the material and subsequent

cracking of the pellets. The swelling can also be observed from the samples' surface where the irradiated, and cracked, region is elevated compared to the rest of the unirradiated area. Swelling caused by the high density of irradiation defects and the implanted hydrogen could have resulted in an effective expansion of the lattice parameter thus reducing the Young's modulus.

## Author contributions

Elina Charatsidou: Conceptualization, Methodology, Formal Analysis, Experimental Investigation, Simulations, Visualization, Writing - original draft. Maria Giamouridou: Conceptualization, Formal Analysis, Experimental Investigation, Simulations, Visualization, Writing - review & editing. Andrea Fazi: Experimental Investigation, Formal Analysis, Visualization, Writing - original draft, review & editing. Gyula Nagu: Experimental Investigation, Formal Analysis, Writing - review & editing. Diogo Ribeiro Costa: Methodology, Formal Analysis, Writing - review & editing. Sarmad Naim Katea: Experimental Investigation, Writing - review. Mikael Jolkkonen: Formal Analysis, Writing - original draft, review & editing. Gunnar Westin: Experimental Investigation, Writing - review & editing. Mattias Thuvander: Formal Analysis, Writing - review & editing. Daniel Primetzhofer: Formal Analysis, Writing - review & editing. Pär Olsson: Conceptualization, Methodology, Formal Analysis, Experimental Investigation, Supervision, Funding Acquisition, Writing - review & editing.

## Declaration of competing interest

The authors declare that they have no known competing financial interests or personal relationships that could have appeared to influence the work reported in this paper.

## Acknowledgements

Financial support from The Swedish Foundation for Strategic Research (SSF, Stiftelsen för Strategisk Forskning) within the SUNRISE Centre, under Grant No. ARC19-0043, as well as from the SAFETY-project, under Grant No. EM16-0031, is gratefully acknowledged by the authors. Support of the operation of the Tandem Accelerator at Uppsala University by the Swedish research Council (Grant Agreement #2019-00191) is gratefully acknowledged by the authors. G. Westin gratefully acknowledges support from the O. E. Nycander Foundation. FIB/SEM specimen preparation for TEM, and TEM imaging were performed at Chalmers Materials Analysis Laboratory (CMAL) and the contribution is gratefully acknowledged by the authors. We would like to thank Fredrik Dehlin for the constructive discussions and proofreading. We would like to thank Dr. Faris B. Sweidan for the FEM simulations and discussion on the results. We are thankful to Dr. Mirva Eriksson, manager of National Facility of Spark Plasma Sintering (SPS) at the Department of Materials and Environmental Chemistry at Stockholm University, for the training and support during the SPS experiments. We would also like to thank Dr. Prasath Babu Revathy Rajan, Hultren Laboratory director, at KTH Royal Institute of Technology, for the training and discussions on the EBSD equipment and results. A big thank you to Dr. Petter Ström, associate senior lecturer/assistant professor, at Department of Physics and Astronomy, Applied Nuclear Physics at Uppsala University, for the help and insightful inputs on the initial trial irradiation runs. We would like to thank Dr. Adrian Iovan, Albanova Nanolab manager, at KTH Royal Institute of Technology, for the training on the AFM equipment and discussion on the results. We would like to thank Dr. Mohammad Sattari for his assistance in the TEM work. Lastly, a big thank you to Jane Bottomley, lecturer in Engineering English Language and Communication for proofreading and providing language insights and assistance.

## Appendix A. Supplementary data

Supplementary data to this article can be found online at https://doi.org/10.1016/j.jmat.2024.01.014.

## References

[1] Ekberg C, Ribeiro Costa D, Hedberg M, Jolkkonen M. Nitride fuel for Gen IV nuclear power systems. J Radioanal Nucl Chem 2018;318(3):1713–25.
[2] Streit M, Ingold F. Nitrides as a nuclear fuel option. J Eur Ceram Soc 2005;25(12):2687–92.
[3] Troyanov VM, Grachev AF, Zabud'ko LM, Skupov MV. Prospects for using nitride fuel in fast reactors with a closed nuclear fuel cycle. At Energy 2014;117(2):85–91.
[4] Dehlin F, Wallenius J, Bortot S. An analytic approach to the design of passively safe lead-cooled reactors. Ann Nucl Energy 2022;169:108971.
[5] Wallenius J, Qvist S, Mickus I, Bortot S, Szakalos P, Ejenstam J. Design of SEALER, a very small lead-cooled reactor for commercial power production in off-grid applications. Nucl Eng Des 2018;338:23–33.
[6] Adamov EO, Kaplienko AV, Orlov VV, Smirnov VS, Lopatkin AV, Lemekhov VV, et al. Brest lead-cooled fast reactor: from concept to technological implementation. At Energy 2021;129(4):179–87.
[7] Youinou GJ, Sen RS. Impact of accident-tolerant fuels and claddings on the overall fuel cycle: a preliminary systems analysis. Nucl Technol 2014;188(2):123–38.
[8] Suzuki Y, Arai Y. Thermophysical and thermodynamic properties of actinide mononitrides and their solid solutions. J Alloys Compd 1998;271–273:577–82.
[9] Hayes SL, Thomas JK, Peddicord KL. Material property correlations for uranium mononitride. III. Transport properties. J Nucl Mater 1990;171(2–3):289–99.
[10] Kikuchi T, Takahashi T, Nasu S. Porosity dependence of thermal conductivity of uranium mononitride. J Nucl Mater 1973;45(4):284–92.
[11] Sunder S, Miller NH. XPS and XRD studies of corrosion of uranium nitride by water. J Alloys Compd 1998;271–273:568–72.
[12] Bailly H, Menessier D, Prunier C. The nuclear fuel of pressurized water reactors and fast reactors design and behaviour. France: Commissariat a l'Energie Atomique; 1999.
[13] Rogozkin BD, Stepennova NM, Proshkin AA. Mononitride fuel for fast reactors. Atom Energy 2003;95(3):624–36.
[14] Matthews RB, Chidester KM, Hoth CW, Mason RE, Petty RL. Fabrication and testing of uranium nitride fuel for space power reactors. J Nucl Mater 1988;151(3):345.
[15] Matthews RB. Irradiation performance of nitride fuels. In: Proceedings of Specialist Conference on Space Nuclear Power and Propulsion Technologies - Materials and Fuels, Podolsk - Moskow, 1993.
[16] Potter RA, Scott JL. Continuation of development of nitrides for space nuclear reactors. Mar [cited 2023 Jul 21]. Report No.: NASA-CR-134498. Available from: https://ntrs.nasa.gov/citations/19750003655; 1974.
[17] Wullaert RA, Lagedrost JF, Bugl J, Gates JE. Radiation stability of uranium mononitride. Columbus, OH (United States): Battelle Memorial Inst.; 1963 Jun [cited 2023 Jul 21]. Report No.: BMI-1638; EURAEC-760. Available from: https://www.osti.gov/biblio/4157389.
[18] Harp JM, Morris RN, Petrie CM, Burns JR, Terrani KA. Post irradiation examination from separate effects irradiation testing of uranium nitride kernels and coated particles. J Nucl Mater 2021;544:152696.
[19] Heidrich B. Roadmap for the application of ion beam technologies to challenges for the advancement and implementation of nuclear energy technologies. United States: Idaho National Lab. (INL), Idaho Falls, ID; 2017 Sep [cited 2023 Jul 21]. Report No.: INL/EXT-17-43130. Available from: https://www.osti.gov/biblio/1408762.
[20] Pakarinen J, He L, Gan J, Nelson AT, El-Azab A, Khafizov M, et al. Proton irradiation-induced blistering in $UO_2$. MRS Adv 2021;6(47):1032–6.
[21] Pakarinen J, He L, Gupta M, Gan J, Nelson A, El-Azab A, et al. 2.6MeV proton irradiation effects on the surface integrity of depleted $UO_2$. Nucl Instrum Methods Phys Res Sect B Beam Interact Mater Atoms 2014;319:100–6.
[22] Pakarinen J, Khafizov M, He L, Wetteland C, Gan J, Nelson AT, et al. Microstructure changes and thermal conductivity reduction in $UO_2$ following 3.9 MeV $He^{2+}$ ion irradiation. J Nucl Mater 2014 Nov 1;454(1):283–9.
[23] He L, Khafizov M, Jiang C, Tyburska-Püschel B, Jaques BJ, Xiu P, et al. Phase and defect evolution in uranium-nitrogen-oxygen system under irradiation. Acta Mater 2021;208:116778.
[24] Xiu P, Jin M, Bawane K, Tyburska-Püschel B, Jaques BJ, Field KG, et al. Dislocation loops in proton irradiated uranium-nitrogen-oxygen system. J Nucl Mater 2021;557:153244.
[25] Ziegler JF, Ziegler MD, Biersack JP. Srim - the stopping and range of ions in matter (2010). Nucl Instrum Methods Phys Res B 2010;268:1818–23.
[26] Malkki P, Jolkkonen M, Hollmer T, Wallenius J. Manufacture of fully dense uranium nitride pellets using hydride derived powders with spark plasma

sintering. J Nucl Mater 2014;452(1–3):548–51.
[27] Malkki P. The manufacturing of uranium nitride for possible use in light water reactors. Licentiate Thesis. KTH Royal Institute of Technology; 2015. TRITA-FYS 2015:25.
[28] Mishchenko Y, Patnaik S, Charatsidou E, Wallenius J, Lopes DA. Potential accident tolerant fuel candidate: investigation of physical properties of the ternary phase $U_2CrN_3$. J Nucl Mater 2022;568:153851.
[29] Johnson KD, Lopes DA. Grain growth in uranium nitride prepared by spark plasma sintering. J Nucl Mater 2018;503:75–80.
[30] Naim Katea S, Westin G. Carbothermal nitridation of solution synthesised $ZrO_2$–carbon nanocomposites; phase-development from precursor to nitride. Ceram Int 2021;47(8):10828–47.
[31] Muta H, Kurosaki K, Uno M, Yamanaka S. Thermal and mechanical properties of uranium nitride prepared by SPS technique. J Mater Sci 2008;43(19):6429–34.
[32] Stoller RE, Toloczko MB, Was GS, Certain AG, Dwaraknath S, Garner FA. On the use of SRIM for computing radiation damage exposure. Nucl Instrum Methods Phys Res Sect B Beam Interact Mater Atoms 2013;310:75–80.
[33] Yang Y, Dickerson CA, Allen TR. Radiation stability of ZrN under 2.6 MeV proton irradiation. J Nucl Mater 2009;392(2):200–5.
[34] Rahman MM, Yamamoto T, Matsumura S, Costantini JM, Yasuda K. Ab initio molecular dynamics study of threshold displacement energy in zirconium nitride. J Nucl Mater 2021;554:153076.
[35] Nagy G, Whitlow HJ, Primetzhofer D. The scanning light ion microprobe in Uppsala – status in 2022. Nucl Instrum Methods Phys Res Sect B Beam Interact Mater Atoms 2022;533:66–9.
[36] Doebelin N, Kleeberg R. Profex: a graphical user interface for the Rietveld refinement program BGMN. J Appl Crystallogr 2015;48(5):1573–80.
[37] Gražulis S, Daškevič A, Merkys A, Chateigner D, Lutterotti L, Quirós M, et al. Crystallography Open Database (COD): an open-access collection of crystal structures and platform for world-wide collaboration. Nucleic Acids Res 2012;40(D1):D420–7.
[38] Hartig SM. Basic image analysis and manipulation in ImageJ. Curr Protoc Mol Biol 2013;102(1):14–15.1. 14.15.12.
[39] Langford RM, Rogers M. In situ lift-out: steps to improve yield and a comparison with other FIB TEM sample preparation techniques. Micron 2008;39(8):1325–30.
[40] Kwong WY, Zhang WY. Electron-beam assisted platinum deposition as a protective layer for FIB and TEM applications. In: ISSM 2005, IEEE international symposium on semiconductor manufacturing. 2005; 2005. p. 469–71.
[41] Costa DR, Liu H, Lopes DA, Middleburgh SC, Wallenius J, Olsson P. Interface interactions in UN-X-$UO_2$ systems (X = V, Nb, Ta, Cr, Mo, W) by pressure-assisted diffusion experiments at 1773 K. J Nucl Mater 2022;561:153554.
[42] Muromura T, Tagawa H. Formation of uranium mononitride by the reaction of uranium dioxide with carbon in ammonia and a mixture of hydrogen and nitrogen— I synthesis of high purity UN. J Nucl Mater 1977;71(1):65–72.
[43] Evans PE, Davies TJ. Uranium nitrides. J Nucl Mater 1963;10(1):43–55.
[44] Hayes SL, Thomas JK, Peddicord KL. Material property correlations for uranium mononitride: I. Physical properties. J Nucl Mater 1990;171(2):262–70.
[45] Poineau F, Yeamans CB, Silva GWC, Cerefice GS, Sattelberger AP, Czerwinski KR. X-ray absorption fine structure spectroscopic study of uranium nitrides. J Radioanal Nucl Chem 2012;292(3):989–94.
[46] Denton AR, Ashcroft NW. Vegard's law. Phys Rev A 1991;43(6):3161–4.
[47] Johnson KD. High performance fuels for water-cooled reactor systems. PhD Thesis. KTH Royal Institute of Technology; 2016. TRITA-FYS 2016:72.
[48] Adachi J, Kurosaki K, Uno M, Yamanaka S, Takano M, Akabori M, et al. Mechanical properties at sub-microscale and macroscale of polycrystalline uranium mononitride. J Nucl Mater 2009;384(1):6–11.
[49] Hayes SL, Thomas JK, Peddicord KL. Material property correlations for uranium mononitride: II. Mechanical properties. J Nucl Mater 1990;171(2):271–88.
[50] Török E, Perry AJ, Chollet L, Sproul WD. Young's modulus of TiN, TiC, ZrN and HfN. Thin solid films 1987;153(1):37–43.
[51] Synthesis Ul-HamidA. Microstructural characterization and nanoindentation of Zr, Zr-nitride and Zr-carbonitride coatings deposited using magnetron sputtering. J Adv Res 2021;29:107–19.
[52] Adachi J, Kurosaki K, Uno M, Yamanaka S. Porosity influence on the mechanical properties of polycrystalline zirconium nitride ceramics. J Nucl Mater 2006;358(2–3):106–10.
[53] Wakita M, Suzuki S. In-situ observation of microstructure change in steel by EBSD. Nippon Steel Sumitomo Metal Tech Rep 2017:32–7. Report No.: 114.
[54] Xi J, Zhang P, He C, Zang H, Guo D, Li T. The role of point defects in the swelling and elastic modulus of irradiated cubic silicon carbide. Nucl Instrum Methods Phys Res Sect B Beam Interact Mater Atoms 2015;356–357:62–8.
[55] Singh G, Koyanagi T, Petrie C, Terrani K, Katoh Y. Evaluating the irradiation effects on the elastic properties of miniature monolithic SiC tubular specimens. J Nucl Mater 2018;499:107–10.

**Elina Charatsidou** obtained her BSc in Physics from AUTh Aristotle University of Thessaloniki in Greece in 2017. She completed her MSc in Nuclear Energy Engineering at KTH Royal Institute of Technology in 2020. She is a PhD student within the SUNRISE Centre for sustainable nuclear energy research in Sweden, at KTH Royal Institute of Technology. She is working with Uranium Nitride (UN) fuel for fast reactors, integrating experiments and modeling analyses. Her research focuses on fabrication of UN fuel, microstructural characterization, separate effect testing, such as ion-beam irradiation, thermal and mechanical testing to investigate the behavior of the fuel under various conditions. Additionally, she is working on electronic structure theory and multi-scale modeling of nitride nuclear fuels. Lastly, Elina Charatsidou is a science communicator and creator of a scientific YouTube channel 'Your Friendly Nuclear Physicist' on public awareness of nuclear energy.